J. Mech. Phys. Solids 159 (2022) 104711

Contents lists available at ScienceDirect

Journal of the Mechanics and Physics of Solids

journal homepage: www.elsevier.com/locate/jmps

Coupled bend–twist mechanics of biomimetic scale substrate

Sanjay Dharmavaram [a], Hossein Ebrahimi [b], Ranajay Ghosh [b,*]

[a] Department of Mathematics, Bucknell University, Lewisburg, PA, USA
[b] Department of Mechanical and Aerospace Engineering, University of Central Florida, Orlando, FL, USA

ARTICLE INFO

Keywords:
Fish scales
Biomimetic
Structure–property
Cosserat
Architected

ABSTRACT

We develop the mechanics of combined bending and twisting deformation of a one-dimensional filamentous structure with protruding stiff fish-scale-like plates embedded at an angle on the surface. We develop a Cosserat kinematic formulation along with scale contact constraints. This geometrically exact model allows us to bypass the limitations of small deflection finite element computations, thereby preserving the accuracy of scale kinematics. The derived structure–property relationships reveal, for the first time, the combined effect of bending and twisting on a slender fish-scale inspired substrate. The model subsumes previous models on pure bending and pure twisting, but also shows previously unobserved phenomena that arise due to the coupled effects of these loads. These include a new interpretation of kinematic locking behavior, multiple contact regimes, asymmetric sensitivities of one curvature over the other, and discontinuous transitions in the nonlinear moment–curvature and torque–twist behaviors, reflecting the complex scale engagement patterns.

1. Introduction

Fishes are synonymous with scales, Fig. 1(a), although scales are far more versatile in nature. They cover numerous reptiles and can also be intermittently found in mammals such as in pangolins and armadillos (Wang et al., 2016; Chen et al., 2011). More interestingly, there are scale-like features in the wings of butterflies, human hair and papillae on feline tongues (LaTorre and Bhushan, 2006; Michielsen and Stavenga, 2008), indicating the singular importance of the scale morphology in enhancing functions. One of the major advantages of scales architecture is that they are generally lightweight additions to a substrate due to low volume fraction, but still enhance stiffness and multifunctionality (Buehler, 2006; Wegst et al., 2015). Several critical properties including protection, locomotion, camouflaging, and thermal regulation have been attributed to scales (Kertész et al., 2008; Long et al., 1996; Song et al., 2010). Thus, they are now intensely studied as material templates to make armors, smart skins, soft robotics and multifunctional surfaces (Sadati et al., 2015; Wei et al., 2016; Roche et al., 2017; Sire et al., 2009). Mechanically, scales give rise to fascinating emergent behavior such as strain stiffening, evolving directionality and anomalous frictional response (Ghosh et al., 2014, 2016, 2017; Ali et al., 2019a,c,b, 2020; Ebrahimi et al., 2019, 2020, 2021a,b). These behaviors can potentially aid organisms in balancing multiple complex, and often contradictory functions such as locomotion with protection, and flexibility with stiffness.

Such possibilities have resulted in numerous studies in the past, to understand the nature of enhancements to material properties brought about by scales. Early research highlighted and confirmed the outstanding behaviors of 1-dimensional beam-like substrates covered uniformly with scales using a combination of analytical and finite element (FE) models (Ghosh et al., 2014; Ebrahimi et al., 2019, 2020; Vernerey and Barthelat, 2010; Vernerey et al., 2014). These works established precise structure–property relationships

* Correspondence to: 4000 Central Florida Blvd, Orlando, FL 32816, USA.
E-mail addresses: sd045@bucknell.edu (S. Dharmavaram), ebrahimi@knights.ucf.edu (H. Ebrahimi), ranajay.ghosh@ucf.edu (R. Ghosh).

https://doi.org/10.1016/j.jmps.2021.104711
Received 24 August 2021; Received in revised form 31 October 2021; Accepted 2 November 2021
Available online 10 December 2021

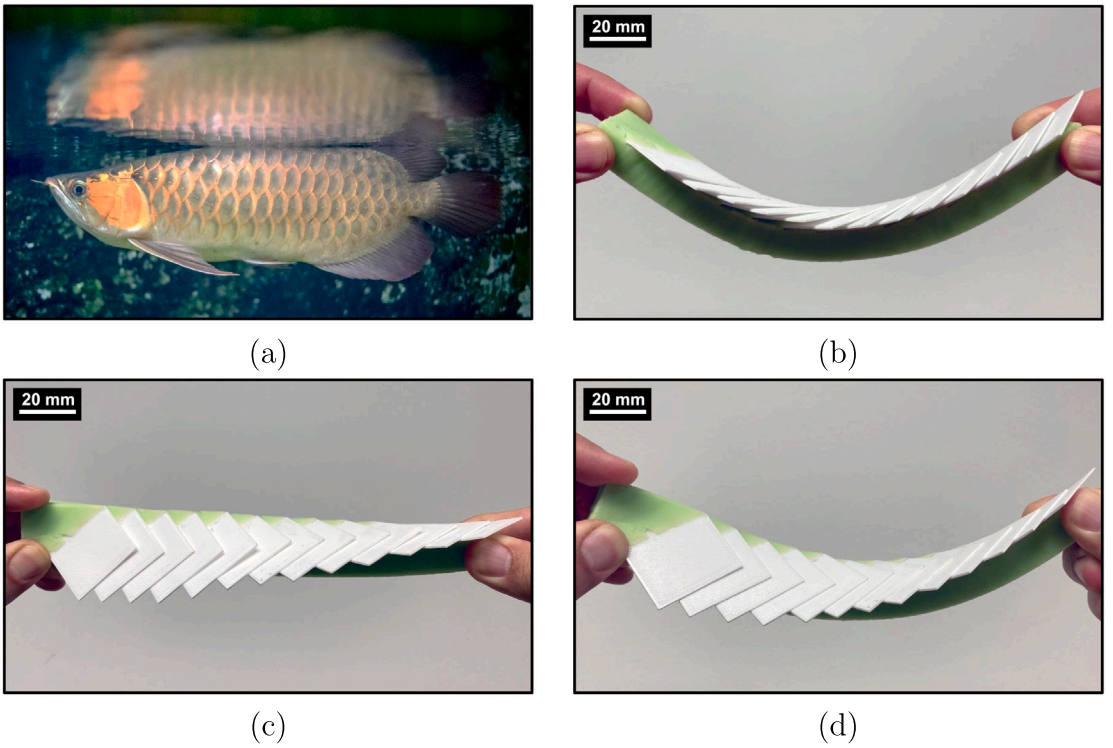

Fig. 1. (a) Natural fish scales under deformation mode, adapted under CC BY 2.0 (Kemoole, 2017). (b) Fabricated biomimetic scale metamaterials under bending deformation. (c) Fabricated biomimetic scale metamaterials under twisting deformation. (d) Fabricated biomimetic scale metamaterials under combined bending and twisting deformation.

in pure bending loads for both smooth and rough sliding between scales, and for both rigid and flexible scales (Ghosh et al., 2014, 2016; Vernerey and Barthelat, 2010, 2014; Martini et al., 2017; Shafiei et al., 2021). The essential characteristics of bending behavior such as strain stiffening and locked states were found to be universally valid even when stiff scales were not uniformly distributed (e.g. functionally graded (Ali et al., 2019c)) or loaded under non-uniform bending (Ali et al., 2019a).

The locked state is essentially a kinematic configuration beyond with scale motion would result in interpenetration leading to rigid behavior. In reality, even before locking commences, the contact forces on the scales would be large enough to lead to scales deformation. Thus, bending behavior would transition from substrate deflection (soft) to scale deformation (stiff), leading to a sharp increase in rigidity of the overall structure. Recent studies have further confirmed locking and nonlinear strain stiffening phenomena under pure torsion, thereby extending their validity even in twisting (Ebrahimi et al., 2019, 2020). However, calculations of structure–property under torsion, while underlining the universality, also highlighted striking differences from bending. For instance, the kinematic locking envelopes are complex nonlinear functions of geometry, unlike in bending where they are linear. In addition, the tilt angle of the scales (see Fig. 1(b) to Fig. 1(d)), had a significant impact on the nature of locking, with some angles even precluding locking behavior. When Coulomb friction was included between the sliding scales, more differences were evident (Ghosh et al., 2016; Ebrahimi et al., 2020). For instance, while frictional locking was observed in both bending and twisting, in the twisting case, locking envelopes were highly nonlinear without any closed form solution, unlike the bending case. Also, the relative energy dissipated due to friction in one cycle of loading (i.e., from unloaded state to locked state) was found to monotonically increase with the friction coefficient (μ) for twisting case, even though for bending case, increasing μ did not always increase the dissipated energy in a cycle (Ebrahimi et al., 2020; Ghosh et al., 2016). Such differences are not unexpected as mechanical behavior is dependent on the interplay of structure, load, and geometry with no intrinsic guarantees on universality. Thus, it is important to investigate individual canonical loading cases carefully and rigorously, before declaring either generalities or anomalies.

It is surprising that the mechanics of combined bending and twisting has not been studied. There is virtually no knowledge of the behavior of slender fish-scale inspired substrates in 3-D or spatial deflections for non-trivial load cases. 3-D deflection under coupled loading is significantly more complex, but of great practical applications. This is both due to the nature of real world loads and also the possibility of geometrical defects in the biomimetic substrate, leading to cross curvatures (e.g. sagging or intrinsic twist). Prior research noted above, indicate that existing models may not be universally valid, scale linearly or even hold similar functional forms across geometry and loading combinations (Ali et al., 2019a,c). Thus, entirely new models are necessary to arrive at structure–property relationships.

We address this lacuna in this work, by developing the mechanics of a frictionless biomimetic scale-covered beam, which its 3D-printed prototype is shown in Fig. 1(b) to Fig. 1(d). Using a Cosserat rod model, we obtain the structure–property relationships and reveal the nature and regimes of nonlinearity, the interplay of bending and twisting, relationships between global (substrate) and local (scale) deformations, and locking behavior. We use finite element (FE) simulations and prior results in the literature to

validate our model. This paper is organized as follows: in Section 2, we develop the kinematics of the filament in bending and twisting loads, and derive the moment–curvature relationships, assuming small strains and additive strain energies. In Section 3, we briefly describe the finite element model we use to validate our theory. In Section 4, we conclude the paper with results and discussion.

2. Contact mechanics of scales engagement

We develop a kinematic description of the scale-covered substrate, which is shown in Fig. 2(a) schematically. The inherent challenge in describing kinematics of this system is the complex 3-D configuration of scales and their rotation with respect to the substrate. We address this by using a Cosserat kinematic description, commonly used to model finite elasticity of rods. Although the structure shown in Fig. 2 has a finite width, any variation of strains along the width (i.e., along the x-direction) has been neglected and we model the substrate as an idealized rod. Cosserat kinematics is convenient, because it incorporates a natural director basis at each point along the rod. We use this basis to describe the orientation of the scale relative to the substrate. In this way, the scales' orientations naturally couple to the bending strain variables of the Cosserat model.

Another advantage of the Cosserat framework is that modeling the mechanics of these structures is straightforward; we add the strain energies of the substrate and the homogenized energy for scales (see Section 2.4). In this work, we will assume small strains in the substrate and use a linearly elastic constitutive law for it. This has been found to be sufficient in the practical contexts of relatively thin substrates that tend to lock before very large strains are permitted (Vernerey and Barthelat, 2014; Ghosh et al., 2014; Martini et al., 2017; Shafiei et al., 2021). More complicated constitutive models can be easily incorporated (Antman, 1995; Audoly and Pomeau, 2010) within our framework. Other simplifying assumptions and the general validity of the energy formulation have been discussed elsewhere (Ebrahimi et al., 2019; Ghosh et al., 2017).

2.1. Global cosserat kinematics

Consider the system shown in Fig. 2(a). We model the substrate as a Cosserat rod (Antman, 1995; Audoly and Pomeau, 2010) whose centroidal curve in its undeformed reference configuration is defined by $\mathbf{R}(s)$, where s represents the arc-length along the undeformed configuration. As shown in the figure, the planar undeformed substrate points along the z-direction, i.e., $\mathbf{R}(s) = s\mathbf{e}_3$, where $\mathbf{e}_1$, $\mathbf{e}_2$, and $\mathbf{e}_3$ are the standard Cartesian basis vectors along the x, y, and z directions, respectively. We identify the reference directors of the undeformed rod ($\mathbf{D}_i,\ i = 1, 2, 3$) with the cartesian basis vectors, i.e., $\mathbf{D}_i = \mathbf{e}_i$. Let $\mathbf{r}(s)$ denote the deformed position of the centroidal curve (shown in Fig. 2(b)), and $\mathbf{d}_1(s)$, $\mathbf{d}_2(s)$, and $\mathbf{d}_3(s)$ are the orthonormal directors moving along the deformed rod. In the Cosserat description, the directors of the deformed configuration are related to those of the undeformed configuration by an orthogonal (rotation) matrix $\mathbf{Q}(s)$:

$$\mathbf{d}_i(s) = \mathbf{Q}(s)\mathbf{e}_i, \text{ for } i = 1, 2, 3. \tag{1}$$

Differentiating (1) with respect to s and substituting for $\mathbf{e}_i$ using the same, we obtain

$$\mathbf{d}_i'(s) = \mathbf{K}\mathbf{d}_i, \text{ for } i = 1, 2, 3, \tag{2}$$

where

$$\mathbf{K} := \mathbf{Q}'(s)\mathbf{Q}^T(s), \tag{3}$$

is a skew-symmetric matrix that depends on the bending and twisting strains in the rod. We can associate $\mathbf{K}$ (written with respect to the basis $\{\mathbf{d}_1, \mathbf{d}_2, \mathbf{d}_3\}$) with an axial vector, $\boldsymbol{\kappa} := \kappa_1\mathbf{d}_1 + \kappa_2\mathbf{d}_2 + \kappa_3\mathbf{d}_3$, i.e.,

$$\mathbf{K} = \begin{pmatrix} 0 & -\kappa_3 & \kappa_2 \\ \kappa_3 & 0 & -\kappa_1 \\ -\kappa_2 & \kappa_1 & 0 \end{pmatrix}. \tag{4}$$

Thus, we can rewrite (2) as

$$\mathbf{d}_i' = \boldsymbol{\kappa} \times \mathbf{d}_i, \text{ for } i = 1, 2, 3. \tag{5}$$

The strain variable κ_3 is interpreted as the twisting strain in the rod, while κ_1 and κ_2 as the bending strains about the x and y axes, respectively. Note that the definition of bending and twisting strains in the Cosserat sense described above is distinct from the actual 3D strains in the substrate. In Cosserat kinematics, the rod is modeled as a 1D curve, and Cosserat strains can be interpreted as the (3D) strains averaged over the cross-section of the substrate (Antman, 1995). This approximation is justified for thin structures. In the cases of pure bending (Ghosh et al., 2014) or pure twisting (Ebrahimi et al., 2019), we can identify the Cosserat strains with the curvature of the rod or twist rate, respectively. However, the matrix description of the strains, noted in (4), is more appropriate for the general case considered here. *Henceforth, we use the term 'strains' strictly in this Cosserat sense*.

We assume spatially homogeneous strains in this model analogous to prior studies (Ghosh et al., 2014; Vernerey and Barthelat, 2010). This makes $\mathbf{K}$ independent of s and helps set up periodicity conditions to extract structure–property relationships. For sharp gradients in strains or functionally graded structures, either local periodicity (Ali et al., 2019c) or a discrete scale-by-scale approach can be used (Ali et al., 2019a). The periodicity condition allows us to study the kinematics using a representative volume element (RVE) of a pair of scales (Ghosh et al., 2014; Vernerey and Barthelat, 2010).

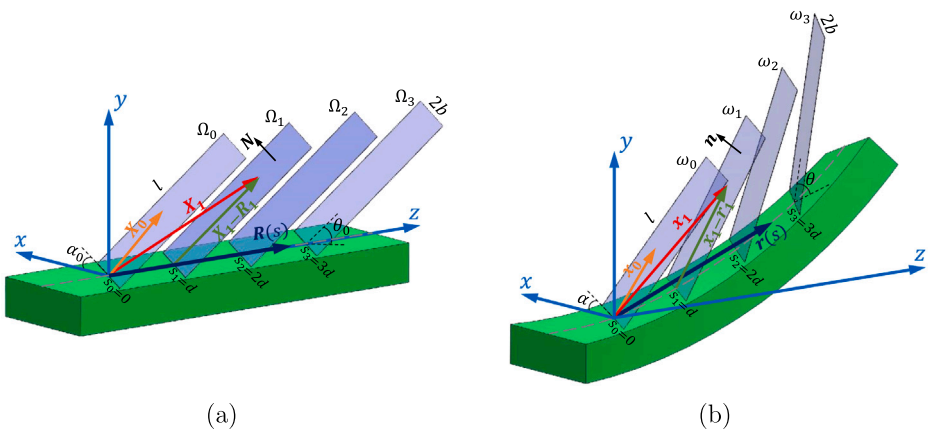

Fig. 2. (a) Schematic of flat reference configuration of the scale-covered rod with arc length variable along the length. (b) Schematic of deformed configuration of the same rod under coupled bend–twist load.

In an RVE, the strain variables κ_1, κ_2, and κ_3 are constant and viewed as parameters. Eq. (3) can be explicitly integrated to solve for $\mathbf{Q}(s)$, and we obtain

$$\mathbf{Q}(s) = e^{s\mathbf{K}}, \tag{6}$$

where without loss of generality, we have assumed that the scale at $s = 0$ is fixed and does not change its orientation as the substrate deforms. That is, $\mathbf{Q}(0) = \mathbf{I}$.

Besides bending and twisting, the rod would, in general, experience shearing in x and y directions, and stretching in the z-direction (we neglect other stretching and shear modes due to the substrate's thin cross-section). In Cosserat kinematics, strain variables associated with the above three modes of deformation are denoted by ν_1, ν_2, and ν_3, respectively. These are related to the deformation by

$$\mathbf{r}'(s) = \sum_{i=1}^{3} \nu_i(s)\mathbf{d}_i(s). \tag{7}$$

If we use (1) to express $\mathbf{d}_i$ in terms of $\mathbf{Q}(s)$ and $\mathbf{e}_i$, and after integrating the resulting equation, we obtain

$$\mathbf{r}(s) = \sum_{i=1}^{3} \int_0^s \nu_i \mathbf{Q}(\tau)\mathbf{e}_i \, d\tau, \tag{8}$$

where we have used the boundary condition $\mathbf{r}(0) = \mathbf{0}$, because the rod is fixed at the origin $s = 0$. In this work, we assume inextensibility and unshearability of the rod and accordingly set $\nu_1 = \nu_2 = 0$ and $\nu_3 = 1$. These are reasonable approximations for the current case as soft polymers under small to moderate loads tend to be incompressible (Chang et al., 1976; Yang et al., 2021). Although some limited warping can take place, their overall effect on the kinematics (but not mechanics) is negligible and has little influence on in-plane shear. For very large twisting, such effects would need to be taken into account (Ebrahimi et al., 2019). In the FE simulations presented in Section 3, we approximate inextensibility by choosing the Poisson's ratio $\nu = 0.49$. Numerical simulations presented in Section 4 seem to confirm this approximation, as we observed no appreciable length change of the rod under the combined loading. Neither was any significant change in cross-sectional area observed. Note that despite these assumptions, there is little loss of generality in the Cosserat framework described below. If the framework were applied in the design and optimization of compressible substrates, the incompressiblity and unshearability assumptions could be easily relaxed. Then, the position of the rod must be determined using (8) with appropriate values for parameters ν_1, ν_2, and ν_3.

2.2. Local kinematics of scales

We assume that the scales are identical in shape (rectangular with scale width $2b$ and scale length $l_s = l + L$, where l is the exposed length, and L is the length of embedded section into substrate), equally spaced along the rod, and are much stiffer than the underlying substrate. The scales are therefore assumed to be rigid. In addition, the assumption of periodicity of contact (i.e., the use of RVEs) is also common (Ghosh et al., 2014; Ebrahimi et al., 2019). Non-periodic or functionally graded systems have been investigated previously for the cases of pure bending and have indicated the salient features of these systems are still preserved under periodicity (Ali et al., 2019a,c). In the reference configuration, the scales are oriented parallel to each other with orientation described by the dihedral angles α_0 and θ_0; see Fig. 2(a). Here, θ_0 is the angle made by the scale with the z-axis, and α_0 is the scale's tilt angle made by its base with the x-axis. The spacing of two adjacent scales measured along the centroidal curve of the undeformed configuration is d. As the rod deforms, the scales rigidly rotate with the rod (maintaining orientations θ_0 and α_0 with the deformed centerline) until contact between adjacent scales occurs. When the scales are in contact, they continue to remain

rigid due to their high stiffness, but the contact induces a change in their orientations, *viz.*, to θ and α due to scale rotation on the substrate.

We now derive conditions for contact between adjacent scales. Let s_i represent the position of the scale i along the arc-length of the undeformed rod. Let $\Omega_i \subset \mathbb{R}^3$ be the set of all points constituting scale i in the reference configuration, and $\omega_i \subset \mathbb{R}^3$ be the set of all points on the same in the deformed configuration. These are shown schematically in Figs. 2(a) and Figs. 2(b), respectively. The midpoint of the base of the scales are located at $\mathbf{R}_i := \mathbf{R}(s_i)$ in the reference configuration and at $\mathbf{r}_i := \mathbf{r}(s_i)$ in the deformed configuration. Note that for given prescribed strains κ_i $(i = 1, 2, 3)$, $\mathbf{r}(s_i)$ is given by (8) where $s_i = i \cdot d$. It is clear from Fig. 2 that for any given $\mathbf{X}_i \in \Omega_i$ and $\mathbf{x}_i \in \omega_i$, the vectors $\mathbf{X}_i - \mathbf{R}_i$ and $\mathbf{x}_i - \mathbf{r}_i$ lie on Ω_i and ω_i, respectively. Let $\mathbf{N}$ be a unit normal to the scale i (in its reference configuration), it then follows that

$$\mathbf{N} \cdot [\mathbf{X}_i - \mathbf{R}_i] = 0. \tag{9}$$

Since the scales rotate rigidly under deformation, we have

$$\mathbf{x}_i - \mathbf{r}_i = \mathbf{Q}_i \left[\mathbf{X}_i - \mathbf{R}_i\right], \tag{10}$$

where $\mathbf{Q}_i := \mathbf{Q}(s_i) = \mathbf{Q}(i \cdot d)$ is the rotation matrix given by (6), evaluated at $s = i \cdot d$. Two adjacent scales (say, $i = 0$ and $i = 1$) in their deformed configurations intersect if and only if they have at least one common point. That is, if and only if the following equation:

$$\mathbf{x}_1 - \mathbf{x}_0 = \mathbf{0}, \tag{11}$$

has at least one solution. Using (10), the previous equation can be equivalently written as

$$\mathbf{r}_1 + \mathbf{Q}_1[\mathbf{X}_1 - \mathbf{R}_1] - \mathbf{X}_0 = \mathbf{0}, \tag{12a}$$

where we have used $\mathbf{Q}_0 = \mathbf{I}$, and $\mathbf{R}_0 = \mathbf{r}_0 = \mathbf{0}$ to account for the fixed boundary condition of scale $i = 0$. Since $\mathbf{X}_0$ and $\mathbf{X}_1$ lie on (finite) planes Ω_0 and Ω_1, respectively, these points must satisfy

$$\mathbf{N} \cdot \mathbf{X}_0 = 0, \text{ for } \mathbf{X}_0 \in \Omega_0, \tag{12b}$$

$$\mathbf{N} \cdot \left[\mathbf{X}_1 - \mathbf{R}_1\right] = 0, \text{ for } \mathbf{X}_1 \in \Omega_1. \tag{12c}$$

Note that solutions $\mathbf{X}_0$ and $\mathbf{X}_1$ of (12) are the 3D coordinates of the points of intersection of the scales, pulled back to the reference configuration. From a computational viewpoint, while it is easy to solve linear system of equations, verifying if the solutions lie on *finite* planes Ω_0 and Ω_1 is not as straightforward. This is because of two factors: (a) finiteness of Ω_1 and Ω_2, and (b) their complicated 3D orientations in $\mathbb{R}^3$. We circumvent both of them by employing the following change of coordinates:

$$\hat{\mathbf{X}}_i := \mathbf{T}[\mathbf{X}_i - \mathbf{R}_i], \ i = 0, 1, \tag{13}$$

where $\hat{\mathbf{X}}_0$ and $\hat{\mathbf{X}}_1$ are rotated coordinate variables and

$$\mathbf{T} = \begin{pmatrix} \cos\alpha & 0 & \sin\alpha \\ 0 & 1 & 0 \\ -\sin\alpha & 0 & \cos\alpha \end{pmatrix}, \tag{14}$$

is a rotation matrix. The transformation rule (13) maps Ω_i to $\hat{\Omega}_i := \mathbf{T}(\Omega_i)$, where the latter's projection on the $\hat{X}_i$-$\hat{Z}_i$ plane is shown in gray in Fig. 3. Thus, $\mathbf{T}$ rotates the scales such that

$$\hat{\Omega}_0 = \hat{\Omega}_1 = \mathcal{B} := [-b, b] \times [0, \infty] \times [0, l\cos\theta]. \tag{15}$$

Rewriting (12) in terms of $\hat{\mathbf{X}}_0$ and $\hat{\mathbf{X}}_1$ and using (13), we obtain the following equivalent conditions for the intersection of the two adjacent scales:

$$\mathbf{T}^T\hat{\mathbf{X}}_0 - \mathbf{Q}_1\mathbf{T}^T\hat{\mathbf{X}}_1 = \mathbf{r}_1, \tag{16a}$$

$$\mathbf{N}^T\mathbf{T}^T\hat{\mathbf{X}}_0 = 0, \tag{16b}$$

$$\mathbf{N}^T\mathbf{T}^T\hat{\mathbf{X}}_1 = 0, \tag{16c}$$

where $\hat{\mathbf{X}}_0, \hat{\mathbf{X}}_1 \in \mathcal{B}$ and superscript T denotes matrix transpose. Thus, transformed variables $\hat{\mathbf{X}}_i$ lie in a simple rectangular domain $\mathcal{B}$. Transforming the variables in this manner also resolves the issue of finiteness noted above, because it is straightforward to check if solutions lie in $\mathcal{B}$ by checking the bounds on the variables.

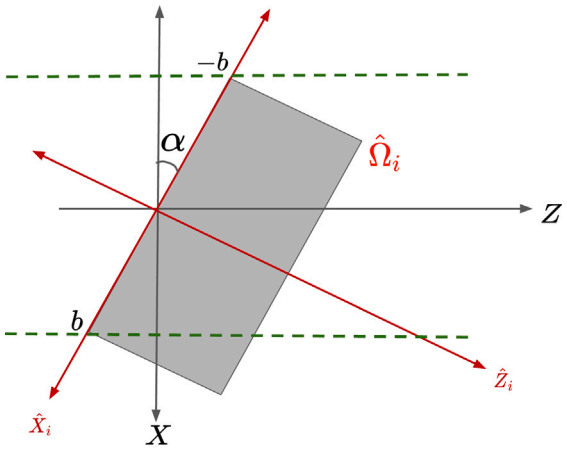

Fig. 3. Schematic showing the coordinate system for $\hat{\mathbf{X}}_i$. The dashed lines represent the edges of the substrate and the gray region is the projection of the scale on the $X-Z$ plane. For each scale i, matrix $\mathbf{T}$ is a coordinate transformation from XYZ to $\hat{X}_i\hat{Y}_i\hat{Z}_i$.

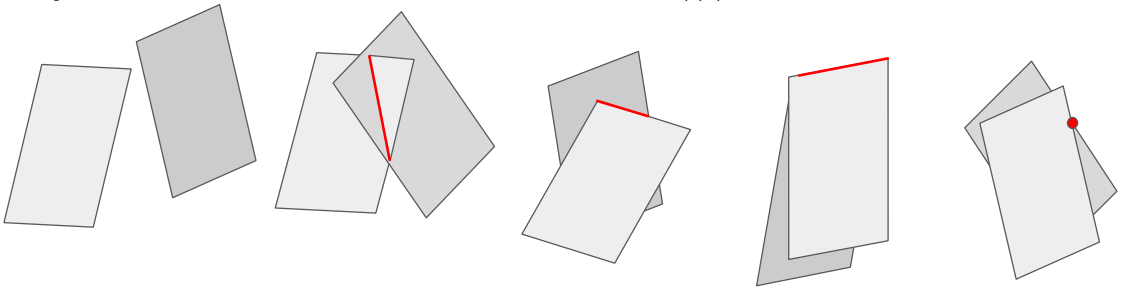

Fig. 4. Various possibilities for two finite rectangles to intersect. The left-most figure shows no contact between scales, the next shows interpenetration of scales. The last three are a non-exhaustive sampling of possible modes of contact. Intersections are shown in red.

2.3. Contact conditions

Observe that (16) is an under-determined linear system with five equations in six unknowns. If $\hat{\mathbf{X}}_0$ and $\hat{\mathbf{X}}_1$ remain unrestricted (i.e., $\hat{\mathbf{X}}_i \in \mathbb{R}^3$, instead of $\mathcal{B}$), then we have two possibilities—no solutions, when the two planes containing the scales are parallel, or infinitely many solutions with a line of intersection. However, since the scales constitute finite planes, since $\hat{\mathbf{X}}_0$ and $\hat{\mathbf{X}}_1$ are restricted to $\mathcal{B}$. When finite planes intersect, there are the following possibilities: (a) no solution, when the planes are either parallel or do not intersect within the domain, (b) infinitely many solutions when the two planes interpenetrate each other with a line-segment intersection (c) *unique or infinitely* many solutions (depending on the relative orientation of the scales), but the scales *do not interpenetrate* each other. The third case is of interest here as such configurations correspond to physically realizable configurations of scales making contact. A schematic for these configurations is shown in Fig. 4 with intersections (if any) shown in red.

There are various ways in which the third case of intersecting yet non-penetrating scales may be realized. Note that for any such configurations there is *at least one point of intersection* that falls into the following two cases: (1) it is either a corner of one of the scales (*corner-contact*) or 2) it is a point of intersection of two edges of different scales (*edge-contact*). See last three figures in Fig. 4. To find the intersection points for the first case, we prescribe corner coordinates $\hat{X}_i$ and $\hat{Z}_i$ (for scale i) and for the second case, we fix two coordinates but from different scales, for instance, $\hat{X}_i$ and $\hat{Z}_j$ ($i \neq j$) are prescribed. We use the bounds for the corresponding variables appearing in (15) to fix these values. Since $\hat{Y}_i$ is unbounded we do not fix this coordinate. The two cases are not mutually exclusive, as some configurations can be both. This happens, for instance, in the third schematic in Fig. 4, where a corner-contact is also an edge-contact. Note that the two cases described above do not automatically exclude interpenetrating configurations. For example, the second schematic in Fig. 4 is an edge-contact. In computations presented below, we exclude such cases by explicitly checking for interpenetration.

There are eight possible corner-contacts depending on which of the eight edges (of the two scales) makes contact with the other. And there are sixteen edge-contacts depending which one of the four edges of first scale makes contact with the four of the other. Of these twenty four possibilities most correspond to configurations with extreme twist or bending that leads to appreciable material nonlinearities, or even cause the scales to debond from the substrate. Therefore, we only consider the following four cases, shown schematically in Fig. 5:

1. Corner-contact: Either of the two top corners of scale '0' makes contact with scale '1'. For such a configuration, we set $(\hat{X}_0, \hat{Z}_0) = (\pm b, l\cos\theta)$. The plus and minus signs signify the two corners. This is shown as red in our schematic Fig. 5(a). In practice, $\hat{X}_0 = -b$ is found only when $\alpha < 0$.

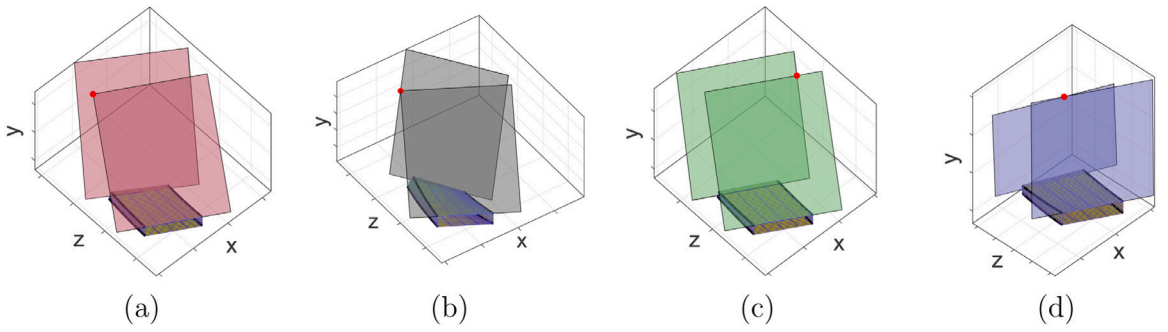

Fig. 5. Modes of contact for an RVE considered in this work: (a) Corner contact (red) (b) Top-left edge contact (black) (c) Top-right edge contact (green) (d) Top edge contact (blue). Contact point is highlighted as a red dot.

2. Top-Left edge contact: This happens when the top edge of scale '0' makes contact with left edge of scale '1'. For this, we set $(\hat{X}_1, \hat{Z}_0) = (-b, l\cos\theta)$. This is shown as black in our schematic; see Fig. 5(b).
3. Top-Right edge contact: This happens when the top edge of scale '0' makes contact with left edge of scale '1'. For this, we set $(\hat{X}_1, \hat{Z}_0) = (b, l\cos\theta)$. This is shown as green in our schematic; see Fig. 5(c).
4. Top edge contact: This happens when the top edge of scale '0' makes contact with top edge of scale '1'. For this, we set $(\hat{Z}_0, \hat{Z}_1) = (l\cos\theta, l\cos\theta)$. This is shown as blue in our schematic; see Fig. 5(c).

These color codes will be used in Section 4 . All the above cases can be expressed mathematically as the conditions

$$\mathbf{a}_0^T\hat{\mathbf{X}}_0 + \mathbf{a}_1^T\hat{\mathbf{X}}_1 = A, \tag{17a}$$

$$\mathbf{b}_0^T\hat{\mathbf{X}}_0 + \mathbf{b}_1^T\hat{\mathbf{X}}_1 = B, \tag{17b}$$

where $\mathbf{a}_0$, $\mathbf{a}_1$, $\mathbf{b}_0$, $\mathbf{b}_1$ are 3D vectors that select appropriate coordinates of $\hat{\mathbf{X}}_0$ and $\hat{\mathbf{X}}_1$ that we wish to fix, and A and B are the bounds on the coordinates. For example, for the case of corner-contact (Case 1) for the choice $(\hat{X}_0, \hat{Z}_0) = (b, l\cos\theta)$, we set $\mathbf{a}_0 = (1,0,0)$ $\mathbf{a}_1 = (0,0,0)^T$, $\mathbf{b}_0 = (0,0,1)$, $\mathbf{b}_1 = (0,0,0)^T$, $A = b$, and $B = l\cos\theta$ in (17a) and (17b). This choice picks coordinates $\hat{X}_0$ and $\hat{Z}_0$, respectively. For Case 2, i.e., $(\hat{X}_1, \hat{Z}_0) = (-b, l\cos\theta)$, we set $\mathbf{a}_0 = (0,0,1)$, $\mathbf{a}_1 = (0,0,0)^T$, $\mathbf{b}_0 = (0,0,0)$, $\mathbf{b}_1 = (1,0,0)^T$, $A = -b$, and $B = l\cos\theta$.

To obtain an implicit expression for the dependence of $\mathbf{K}$ (and therefore, κ_1, κ_2 and κ_3) on θ, we solve (16) simultaneously with (17a) and (17b). We do this in the following steps. First, we solve (16a) for $\hat{\mathbf{X}}_1$, i.e., $\hat{\mathbf{X}}_1 = \mathbf{T}\mathbf{Q}_1^T\mathbf{T}^T\hat{\mathbf{X}}_0 - \mathbf{T}\mathbf{Q}_1^T\mathbf{r}_1$. We then plug the previous expression for $\hat{\mathbf{X}}_1$ into (17a) and (17b) and obtain equations only involving $\hat{\mathbf{X}}_0$. Taking the resulting equations together with (16b), we obtain a 3×3 system of linear equations $\mathbf{A}\hat{\mathbf{X}}_0 = \mathbf{c}$, where

$$\mathbf{A} = \begin{pmatrix} (\mathbf{T}\mathbf{N})^T \\ (\mathbf{a}_0 + \mathbf{T}\mathbf{Q}_1\mathbf{T}^T\mathbf{a}_1)^T \\ (\mathbf{b}_0 + \mathbf{T}\mathbf{Q}_1\mathbf{T}^T\mathbf{b}_1)^T \end{pmatrix}, \quad \mathbf{c} = \begin{pmatrix} 0 \\ A + \mathbf{a}_1^T\mathbf{T}\mathbf{Q}_1^T\mathbf{r}_1 \\ B + \mathbf{b}_1^T\mathbf{T}\mathbf{Q}_1^T\mathbf{r}_1 \end{pmatrix}. \tag{18}$$

Plugging the solution $\hat{\mathbf{X}}_0 = \mathbf{A}^{-1}\mathbf{c}$ along with the solution $\hat{\mathbf{X}}_1 = \mathbf{T}\mathbf{Q}_1^T\mathbf{T}^T\hat{\mathbf{X}}_1 - \mathbf{T}\mathbf{Q}_1^T\mathbf{r}_1$ in (16c), we obtain the following implicit dependence of θ in terms of $\mathbf{K}$:

$$f(\mathbf{K},\theta) = \mathbf{N}^T\mathbf{Q}_1^T\mathbf{T}^T\mathbf{A}^{-1}\mathbf{c} - \mathbf{N}^T\mathbf{Q}_1^T\mathbf{r}_1 = 0. \tag{19}$$

The dependence of f on $\mathbf{K}$ and θ can be noted by observing that $\mathbf{Q}_1$ and $\mathbf{r}_1$ depend on $\mathbf{K}$ (cf. (6) and (8)), and $\mathbf{N}$, A, and B depend on θ. Parameter α appears in $\mathbf{T}$, while l and b appear in A and B. Eq. (19) is a highly nonlinear 'bridging' law, linking the local to the global kinematics, thus completing the multiscale kinematics description of the system. We solve this equation numerically to obtain the dependence of θ on the bending strains, κ_1, κ_2, and κ_3. Solutions corresponding to interpenetrating configurations are discarded.

2.4. Mechanics of biomimetic scales on slender substrate

In order to understand the mechanics of this structure, we take recourse to energy balance between the global loads and local deformation. We model the underlying substrate as an Euler elastica whose strain energy is given by:

$$\mathcal{E}_{beam} = \int_0^L \left[\frac{1}{2}B_1\kappa_1^2 + \frac{1}{2}B_2\kappa_2^2 + \frac{1}{2}D\kappa_3^2\right] ds. \tag{20}$$

where B_1, B_2 and D are, respectively, the bending and twisting rigidities. For beams with circular cross sections, $B_1 = EI_1, B_2 = EI_2$ and $D = GJ$ where E is the Young's modulus, I_1, I_2 are the respective area moments, G is the shear modulus, and J is the polar moment. In our case, two complications arise. The embedding of the scales lead to an inclusion effect on the beam contributing

to additional stiffness (composite effect). For bending deformation, we postulate a scaling parameter C_f to the bending rigidities, i.e., $B_1 = C_f EI_1, B_2 = C_f EI_2$. The values of the parameter C_f can be obtained using FE simulations (Ebrahimi et al., 2019). For twisting deformation, a non-circular cross section also introduces a warping effect. Although warping is not substantial to affect the kinematics of the scales engagement, it does have an effect on the energy. This is addressed using another multiplicative factor C_w, which is readily available in handbooks (Ugural and Fenster, 2011), and is often scaled with respect to EI_1 rather than GJ. Thus, the twisting rigidity takes the form $D = C_f C_w EI_1$.

To include the strain energy contribution due the scales, we note that a scale's rotation is captured by the angles θ and α. As the substrate deforms under applied strain, the scales rotate freely until a critical threshold of curvatures is reached when the scales engage. Let $\Gamma_e \subset \mathbb{R}^3$ denote the bending strains $(\kappa_1, \kappa_2, \kappa_3)$, for which the scales are engaged. This *engagement region* can be determined by solving (19) for κ_1, κ_2 and κ_3 for which $\theta > \theta_0$, i.e., when scales are in contact. We determined this region numerically. In Fig. 10 of Section 4, we show a plot for a slice of Γ_e along $\kappa_2 = 0$. It is clear that the region depends on geometric parameters l, b, θ_0, etc. Since the scales are built into the substrate, under engagement (i.e., when scales make contact), their rotations are resisted by the substrate. We model the substrate resistance using linear torsional springs with the elastic energy stored in the springs for each scale given by:

$$\mathcal{E}_{scale}(\theta, \alpha) = \frac{1}{2d}\left[K_\theta(\theta - \theta_0)^2 + K_\alpha(\alpha - \alpha_0)^2\right] H_{\Gamma_e}(\kappa_1, \kappa_2, \kappa_3), \tag{21}$$

where K_θ and K_α are spring constants of the torsional springs, and H_{Γ_e} is the indicator function on Γ_e (i.e., $H_{\Gamma_e}(\kappa_1, \kappa_2, \kappa_3) = 1$, if $(\kappa_1, \kappa_2, \kappa_2) \in \Gamma_e$, and zero, otherwise). The total energy per RVE can be additively written as:

$$\mathcal{E}(\kappa_1, \kappa_2, \kappa_3) = \mathcal{E}_{beam}(\kappa_1, \kappa_2, \kappa_3) + \mathcal{E}_{scale}(\theta, \alpha). \tag{22}$$

The change in α, has been quantified previously for pure twisting, in both frictional and frictionless sliding, and was found to be $< 0.8\%$, which is assumed to hold here as well. This is borne out of our current FE simulations which also show similar trends ($\frac{\alpha - \alpha_0}{\alpha_0} \approx 0.8\%$). (Ebrahimi et al., 2019). Therefore, our FE simulations show that the change in α from α_0 is minimal even when the scales are engaged. This observation is in agreement with our earlier findings for the cases of pure bending and twisting (Ghosh et al., 2014; Ebrahimi et al., 2019). We therefore drop its dependence from $\mathcal{E}$ and henceforth fix α to α_0. Note that in light of (19), θ is itself a function of $(\kappa_1, \kappa_2, \kappa_3)$, hence the dependence of $\mathcal{E}$ on the same.

K_θ is related to the Young's modulus of the substrate (E), scale thickness (t_s), inclusion length (L) and θ_0. As we have shown in Ghosh et al. (2014), Ebrahimi et al. (2019) the following non-dimensional scaling exists:

$$\frac{K_\theta}{Et_s^2} = C_B \left(\frac{L}{t_s}\right)^n f(\theta_0), \tag{23}$$

where n is non-dimensionless constant, C_B is a constant, and $f(\theta_0)$ is function of angle θ, that we estimate using FE simulations. For the results presented below, these were $C_B = 3.62$, $n = 1.55$, $f(\theta_0) \approx 1$ (Ebrahimi et al., 2019, 2020).

The bending moments are obtained by differentiating (22) with respect to κ_1, κ_2, and κ_3:

$$M_1 = C_f EI_1\kappa_1 + \frac{K_\theta}{d}(\theta - \theta_0)\frac{\partial\theta}{\partial\kappa_1} H_{\Gamma_e}(\kappa_1, \kappa_2, \kappa_3), \tag{24a}$$

$$M_2 = C_f EI_2\kappa_2 + \frac{K_\theta}{d}(\theta - \theta_0)\frac{\partial\theta}{\partial\kappa_2} H_{\Gamma_e}(\kappa_1, \kappa_2, \kappa_3), \tag{24b}$$

$$M_3 = C_f C_w GI_1\kappa_3 + \frac{K_\theta}{d}(\theta - \theta_0)\frac{\partial\theta}{\partial\kappa_3} H_{\Gamma_e}(\kappa_1, \kappa_2, \kappa_3). \tag{24c}$$

Once $\theta(\kappa_1, \kappa_2, \kappa_3)$ is computed numerically by solving (19), the moments are also computed numerically using (24) to obtain the moment–curvature relationships. Note that the derivative of the indicator function, H_{Γ_e} is the (surface) Dirac Delta distribution which is zero everywhere except on the boundary of Γ_e. This term does not appear in (24) because it is multiplied by $\theta - \theta_0$, which regularizes to zero precisely on the boundary of Γ_e.

3. Finite element analysis

We build Finite Element (FE) models on ABAQUS/CAE 2017 (Dassault Systèmes) to validate the (semi-)analytical model developed above. In simulations, we model the substrate and scales as 3D deformable solids. The substrate is a rectangular prismatic beam (length $L_B = 200$ mm) onto which a row of 19 identical scales are embedded on one side. In this assembly, scales are spaced $d = 10$ mm apart, oriented with angle of $\theta_0 = 5°$ with respect to the substrate's top surface, and angle of $\alpha_0 = 30°$ with respect to the substrate's rectangular cross section. Since our analytical model applies to an RVE, where strains are constant, we chose the substrate to be sufficiently long so as to avoid edge effects. The substrate was modeled as a linear elastic material with an elastic modulus $E_B = 2.5$ MPa and Poisson's ratio $\nu = 0.49$. Thus, the shear modulus of the substrate is $G_B = \frac{E_B}{2(1+\nu)} = 0.84$ MPa. Scales were modeled to be rigid with respect to the substrate by imposing rigid body constraints. The contact between the scales was modeled using 'Surface to Surface Contact' algorithm in ABAQUS (Abaqus, 2014). This algorithm is commonly used for biomimetic scale problems of this type (Ghosh et al., 2014; Ali et al., 2019a,c; Ebrahimi et al., 2019).

The mechanical loads for bending and twisting were applied as boundary conditions quasi-statically to the system. In our numerical studies, we set $\kappa_2 = 0$. That is, we do not explore bending in the transverse direction to the substrate, which is considered trivial in the current context. To compare the combined effect of bending (with strain κ_1) and twisting (with strain κ_3) with the analytical model presented above, we performed the simulation in two static steps with nonlinear geometry option (NLGEOM

on) (Abaqus, 2014). In the first step, bending rotations with the equal magnitude but opposite directions were prescribed to cross-sections at either ends. The magnitude of these rotations were increased linearly from 0 to (approximately) $\kappa_1 L_B/2$, where L_B is the length of the substrate. Due to edge effects, the final value was only approximately a constant throughout the beam. To ameliorate these effects we extracted an averaged strain in the beam far from the ends. More details on this procedure will be explained in A. In the second step, bending rotations were fixed at the final value ($\approx\kappa_1 L_B/2$) and the twisting rotations were applied to the cross-section at either ends with reverse directions, again linearly increasing from 0 to (approximately) $\kappa_3 L_B/2$ during the step time. A frictionless surface-to-surface contact was applied to the scales surfaces. To test the reliability of the numerical results, we carried out a mesh convergence study.

Sufficient mesh density was found for different regions of the model confirming computational accuracy. Mesh convergence led to a total number of about 230,000 elements. Because of the complex geometry of the system particularly due to scale-inclusions in the substrate, the top layer of substrate was meshed with tetrahedral quadratic elements C3D10 and other regions were meshed with quadratic hexahedral elements C3D20. We used nearly incompressible assumption to approximate the behavior of silicone rubbers. In this study we used a combination of C3D20 and C3D10 fully integrated elements in ABAQUS which could be prone to volumetric locking. However, we checked for the classic checkerboard pattern of pressure that is typically a good indicator for the onset of numerical locking (Sheen et al., 2021). Furthermore, we repeated some of our simulations of scale covered beam using reduced order elements (C3D20R), and hybrid (mixed) formulation elements (C3D20H and C3D10H), which also gave nearly identical results.

4. Results and discussion

In this section we present results exploring cross-curvature effects, with various types of scales contact color-coded differently in the plots. Without loss of generality, we take the initial scale angle $\theta_0 = 0°$ (grazing scales) since we are more interested in scale engagement behavior. Scales with $\theta_0 > 0$ would only shift the plots horizontally until engagement occurs, with the curves thereafter following the same trajectories (Ghosh et al., 2014; Ebrahimi et al., 2019). We use the non-dimensional parameters, $\eta = l/d$, $\beta = b/d$, and $\hat{\kappa}_i = \kappa_i d$, $i = 1, 2, 3$, to explore the effects.

A typical $\hat{\kappa}_3$ (twist) versus θ (scale angle) behavior (for a given $\hat{\kappa}_1$) is shown in Fig. 6. In this figure, we set $\hat{\kappa}_1 = 0.23$, $\eta = 3$, $\beta = 1.25$ and $\alpha = 30°$. The presence of an initial bending leads to additional scale contact types, not observed for pure twisting investigated previously (Ebrahimi et al., 2019, 2020). The curves representing various contact regimes, which are color coded in the figure as follows: the black curve is the contact type where the top edge of the first scale makes contact with the left edge of the second, the red curve represents configurations where the corner of the first scale makes contact with the face of the second scale, green curve is the configuration where the top edge of the first scale makes contact with the right edge of the second scale, and the blue curve represents the configuration where the top edges of the two scales make contact; see Fig. 5 for a schematic representation of these various modes. We also provide animations of the contact kinematics (see Supplementary data in Appendix B) for better visualization of this system.

Recall that in the case of pure twisting (Ebrahimi et al., 2019) or pure bending (Ghosh et al., 2014), the kinematic locking is typically identified when the slope of the curve in the strain (curvature/twist)–angle plot goes to infinity. However, in the case of combined load, locking occurs when the slopes changes sign abruptly from positive to negative. This critical point is indicated by a blue triangle in Fig. 6, where the curve is predicted to transition from green to red. Continuously increasing the strain $\hat{\kappa}_3$ at this point would cause the scales to interpenetrate each other. This critical point is thus interpreted as locking. This non-orthogonal condition of locking is a unique artifact of combined load system, not found in pure bending or twisting (Ghosh et al., 2014; Ebrahimi et al., 2019). In the subsequent analysis, we treat post-locking configurations as forbidden. For the parameter values explored in this work, we find that the blue curves (which correspond to configurations with top edge contact) always occur as locked states. Hence, they are not explicitly shown in the figures below. In addition, contact regimes that correspond to very high twisting strains are also not considered as they are of little practical significance and difficult to achieve without introducing significant material nonlinearity.

We now explore in detail the cross-coupling effects of the two bending strains. In Fig. 7(a), we show the effect of bending ($\hat{\kappa}_1$) on the twisting ($\hat{\kappa}_3$) versus scale angle (θ). The various values of $\hat{\kappa}_1$ are shown beside their corresponding curves. This figure is fundamentally different from pure bending (Ghosh et al., 2014) or twisting (Ebrahimi et al., 2019) kinematics. Here, there are distinct regions of kinematics, and they are dependent on the existing bending curvature, with distinct contact regimes emerging throughout the engagement. Thus the existence of bending can result in an entirely new type of kinematic behavior in twisting. The color-coded plots are an indication that there would be kinks in twisting rigidity as contact regimes between scales change as depicted in Fig. 6 (inset C and D). This plot can also be used to note the sensitivity of twisting to existing bending strains. We find that the sensitivity is quite high, and thus any unintended bending either due to sample processing or loading asymmetries can drastically change the overall kinematics. Another remarkable feature is that the locking angle for the scale seems to be insensitive to bending. Hence, the locking envelopes computed from pure twisting would still hold in this case. Overall, bending strains have a differential effect on the twisting kinematics, affecting the kinematics trajectory substantially while leaving the locked state unchanged.

In the same spirit, in Fig. 7(b), we highlight the effect of twisting on the bending behavior of the biomimetic scale beam. Here, we find that a twist in the system also significantly impacts the bending behavior. The bending engagement occurs earlier with an increasing positive twist, whereas the opposite occurs with a negative twist. This trend reflects that twisting on one side has an 'opening' effect on the scale, where they move apart from each other compared to the other side, leading to a 'closing' effect. The slopes also change significantly, indicating a potential impact on the overall stiffness of the system. The abrupt changes correspond to sudden changes in contact regimes and are shown with different colors. Interestingly, the presence of twist does not affect the locking angle, analogous to the twisting case.

The validation of these analytical results using FE models is discussed next. Fig. 7(c) and (d) are the counterparts of Fig. 7(a) and (b), respectively. In Fig. 7(c), we compare the FE results (shown as solid lines with point markers) with the results of our

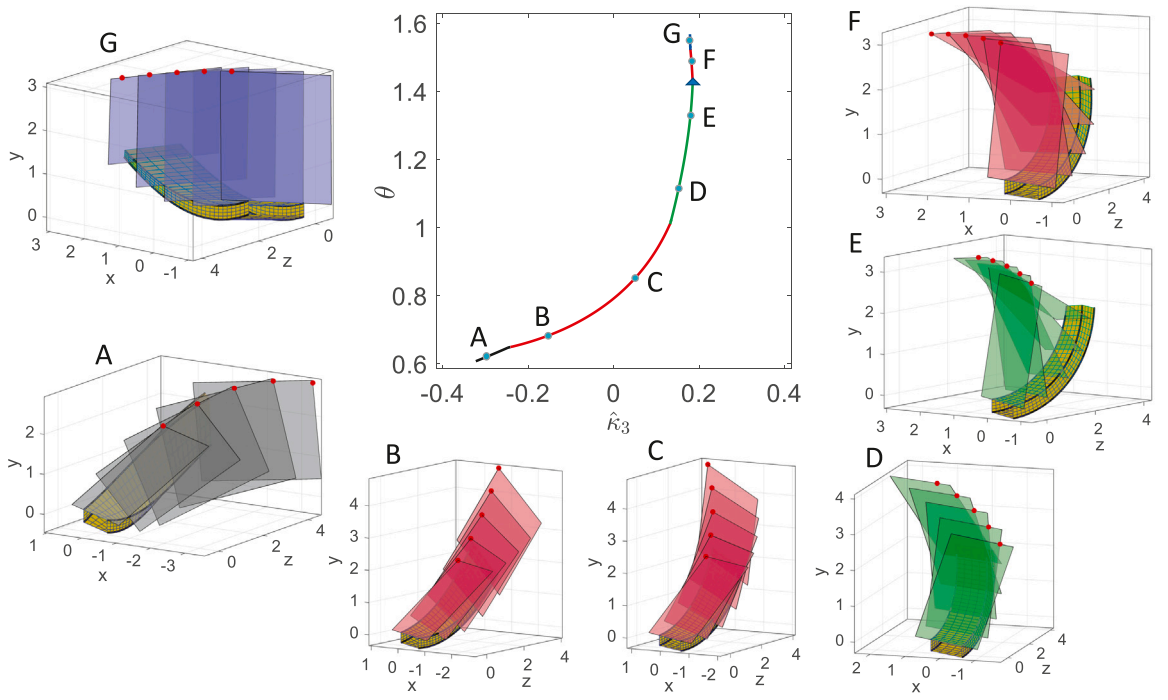

Fig. 6. $\hat{\kappa}_3$ vs θ with different modes of contact. Here the fixed parameters are: $\hat{\kappa}_1 = 0.23$, $\eta = 3$, $\beta = 1.25$ and $\alpha = 30°$. Modes of contact have been depicted with different colors: Red color in the plots shows the corner contact. Black color in the plots shows the Top-left edge contact. Green color in the plots shows the top-right edge contact. Blue color in the plots shows the Top edge contact.

model (shown as dotted lines) for various values of pre-set bending strains ($\hat{\kappa}_1$) in the substrate. The kinks seen in the curves (close to $\hat{\kappa}_3 = 0.05$) are precisely the transition from red to green curves shown in Fig. 7, when the mode of contact changes. Analogous results for θ versus $\hat{\kappa}_1$ for different values of pre-set twisting strains $\hat{\kappa}_3$ are shown in Fig. 7(d). Note that the pre-set strains for the two sets of simulations are approximate. This is because when the second quasi-static step (see Section 3) is performed, the strain values fixed during the first quasi-static step do not remain exactly fixed. That is, as we twist a pre-bent beam, the bending curvatures change mildly under the twisting deformation. In Fig. 7(c) and (d), we account for this change by interpolating over the changing values of $\hat{\kappa}_1$ and $\hat{\kappa}_3$, respectively.

We now use our model to explore the twisting kinematics at a given bending strain, with changing geometric parameters, α and η. These parameters have shown to be critical in dictating the overall kinematics of pure twisting (Ebrahimi et al., 2019). For this, we fix the bending curvature at $\hat{\kappa}_1 = 0.1$. First, we probe the significance of overlap ratio η on the overall kinematics of the system. In Fig. 8(a), we plot θ vs $\hat{\kappa}_3$ for different values of η (for $\beta = 1.25$, $\alpha = 30°$ and $\kappa_1 = 0.15$). Here, we first note the similarities with the pure twisting case. Like pure twisting, increasing η leads to steeper slopes in the $\theta - \hat{\kappa}_3$ plots. However, the twist completely changes the kinematic trajectories by introducing two distinct contact regimes. The abrupt changes in contact are more apparent for lower overlap ratio but are ameliorated at higher overlaps. Note that the plots continue to increase in steepness on the right side until the locked states are reached. On the other hand, on the left side (negative twist), they decrease in slope (flatten) till they collapse into a point. This is the point of disengagement ($\kappa_3 = \kappa_3^*$) of the scales beyond which they no longer remain in contact. A surprising outcome of this plot is that the disengagement point seems to be independent of the overlap ratio. This can be understood if this point is visualized for an RVE, Fig. 9 (intersection between the two scales is shown in red). Evidently, at this point, the nature of contact is the entire edge of one scale moving over the adjacent one. Thus at κ_3^*, η is not well defined, and the scale angle is purely determined by the dihedral angle of two adjacent intersecting planes dependent only on the applied strains.

We see here again that η influences the angle of locking. Furthermore, we find that this parameter has a significant role in determining the system's overall kinematics. Increasing η leads to an overall stiffer nonlinearity but at the same time can potentially change the overall contact regime sequence up until scales lock.

Next, In Fig. 8(b), we plot θ vs $\hat{\kappa}_3$ for different values of α (for $\beta = 1.25$, $\eta = 3$ and $\hat{\kappa}_1 = 0.1$). The effect of the tilt angle α is dramatic for relatively small angles, i.e., $\alpha < 20°$, there is a relatively 'stiff' response on either direction of twisting. These reflect scales sliding in either direction of twisting. However, there is a marked anisotropy between the directions in both magnitude and contact regimes. More interestingly, such bi-directionally distinct stiffness disappears altogether at higher tilt angles, indicating the scales do not or only weakly engage in other directions. The lack of engagement in the other direction can be seen as 'opening' of the scales in one direction versus closing. The effect of α on locking is also pronounced. At lower tilt angles, the stiffening effect disappears into a lockless behavior. This is due to scales sliding past each other without ever satisfying the contact constraints. Locking behavior emerges again for higher tilt angles.

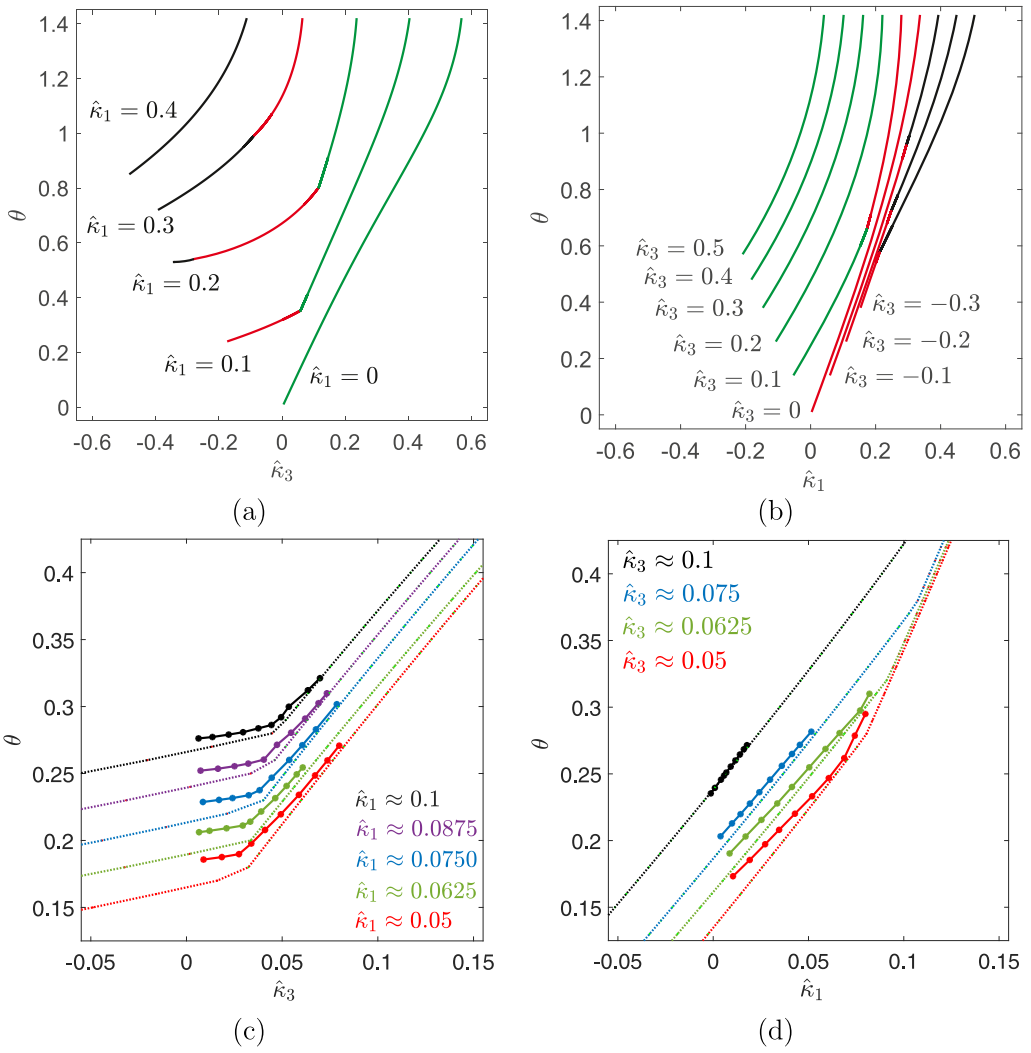

Fig. 7. (a) Analytical results of θ versus $\hat{\kappa}_3$ for different values of bending strains ($\hat{\kappa}_1$). (b) Analytical results of θ versus $\hat{\kappa}_1$ for different values of twisting strains ($\hat{\kappa}_3$). (c) FE results (solid line with point markers) vs analytical results (dotted lines) of θ versus $\hat{\kappa}_3$ for different values of bending strains ($\hat{\kappa}_1$). (d) FE results (solid line with point markers) vs analytical results (dotted lines) of θ versus $\hat{\kappa}_1$ for different values of twisting strains ($\hat{\kappa}_3$). Given parameters are $\eta = 3$, $\beta = 1.25$ and $\alpha = 30°$. In subfigures (a) and (b), modes of contact have been depicted with different colors: Red color shows the corner contact. Black color shows the Top-left edge contact. Green color shows the top-right edge contact.

In Fig. 8(c), we now look at the sensitivity of the bending kinematics in the presence of twist. For these plots, we keep the geometry of the substrates the same and now impose a twist of $\hat{\kappa}_3 = 0.1$ before bending and keep the tilt angle $\alpha = 30°$. Here, we see that the overall impact of higher η is to increase the slope of $\theta - \hat{\kappa}_1$ plot, similar to pure bending (Ghosh et al., 2014). However, the presence of twist changes the nature of the $\theta - \hat{\kappa}_1$ curve by introducing different contact regimes, very similar to the twisting case discussed earlier (Fig. 8(a)). Similar to that case, the abruptness of the kinks diminish at higher η, disappearing altogether when $\eta = 5$. Thus, the higher-scale overlap has a suppressing effect on contact regime transitions. Interestingly, the scales remain engaged even at a negative bending strains, due to the 'closing' effect on the scales due to twisting, where they are pushed closer to each other. However, eventually, the scales again lose contact as bending in the other direction increases sufficiently, once again exhibiting the 'convergence' at the point of disengagement described previously.

We also investigate the effect of an existing twist on $\theta - \hat{\kappa}_1$ relationship for various tilt angles α but with fixed $\eta = 3$ in Fig. 8(d). Here, we find that the contact regime transition is absent at a lower tilt angle, appearing as the tilt angle increases. This shows that the tilt angle is an important parameter that controls the complexity of contact regimes. Overall, the effect of pre-twist in bending is muted at lower tilt angles and higher overlap and more pronounced otherwise.

The investigation above set the stage to investigate the positive–negative effects of twist–bend combinations. Next, we compute the curvature dependence of scale angles for a biomimetic scale beam of fixed geometric parameters to put these bend–twist kinematics in a more general context. This results in a phase plot as shown in Fig. 10. The curvature limits are taken to maintain

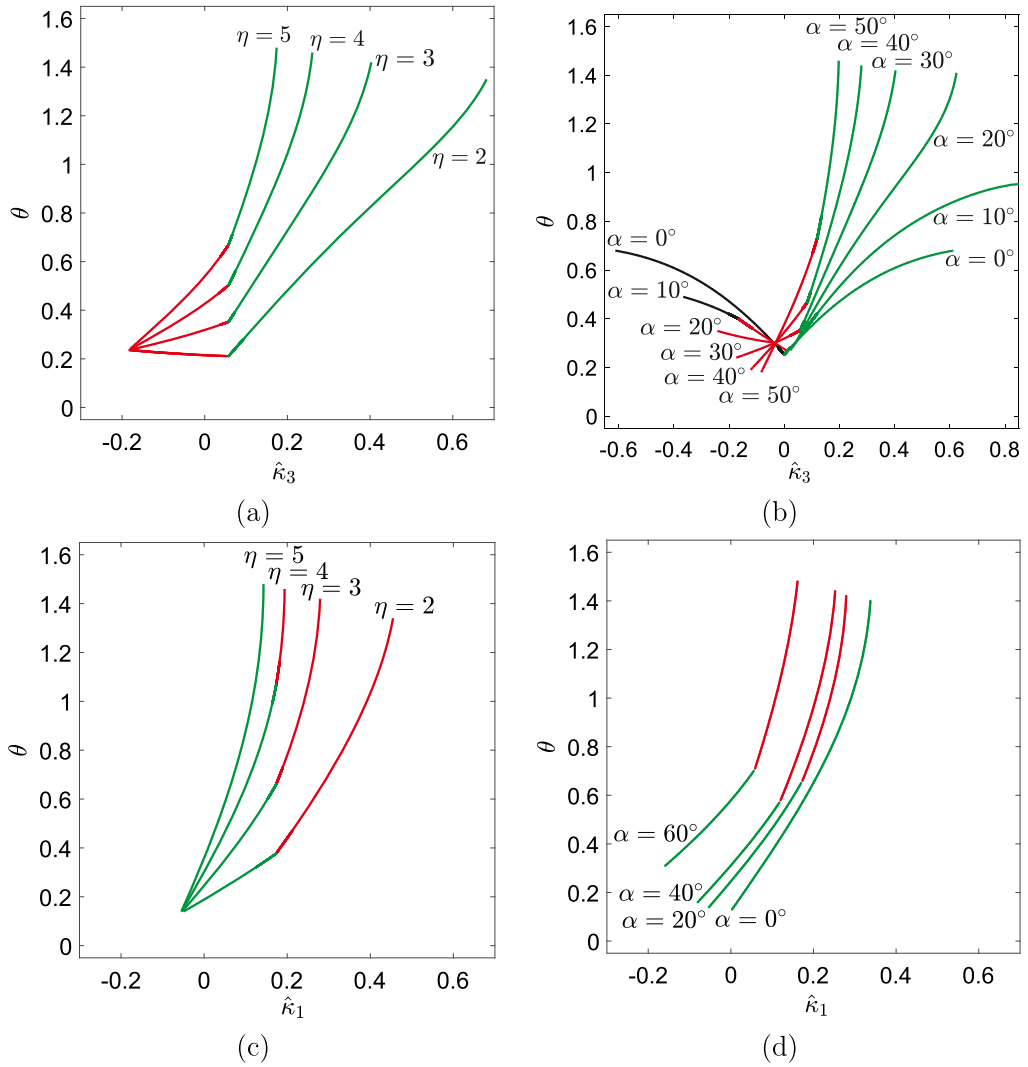

Fig. 8. (a) θ versus $\hat{\kappa}_3$ for different values of η (for $\beta = 1.25$, $\alpha = 30°$, $\hat{\kappa}_1 = 0.1$). (b) θ versus κ_3 for different values of α ($\eta = 3$, $\beta = 1.25$, $\kappa_1 = 0.1$). (c) θ versus κ_1 for different values of η (for $\beta = 1.25$, $\alpha = 30°$, $\kappa_3 = 0.1$). (d) θ versus κ_1 for different values of α ($\eta = 3$, $\beta = 1.25$, $\kappa_3 = 0.1$). In the plots, modes of contact have been depicted with different colors: Red color shows the corner contact. Black color shows the Top-left edge contact. Green color shows the top-right edge contact.

self-consistency for contact regimes studied. For higher twist levels, more contact possibilities would need to be included. The phase plot in Fig. 10 is by solving the kinematic relationships developed earlier connecting scale angles and curvatures numerically at various values of bending and twisting strains.

The phase boundary on the left is the limit of engagement, i.e., we do not have any scales engagement beyond this boundary. The phase boundary on the right-hand side is the locking boundary. Any $(\hat{\kappa}_1, \hat{\kappa}_3)$ combination is forbidden in this region. Thus, the region in between indicates the region of engagement. It is interesting to note that there is no inherent symmetry between bending and twisting. In other words, the effect of bending on twisting is fundamentally different from the converse. In addition, one can see that multiple bend–twist combinations can give rise to the same scale angles. This angular degeneracy is quite remarkable and could have significance for inverse designs.

Finally, we discuss the mechanical behavior of these systems. In Fig. 11(a), we plot bending moment vs. bending strains and discover the role played by the presence of twist for a given η. Higher values of positive twists shift the engagement to earlier parts, whereas higher values of negative twists shift it in the opposite direction. Interestingly, unlike smooth plots seen for pure bending earlier (Ghosh et al., 2014), twist effectively changes the contact regime in terms of discontinuities and jumps in the plot indicating sudden changes in bending rigidity. When a twist is added in the positive direction, the neutral position (no bending strain) is fully engaged (due to the engagement brought about by the twist). The FE comparison with these plots is shown in Fig. 11(b). Notice the validation region is for much smaller values of bending and twisting. This is due to the inherent limitation of traditional FE software in simulating this type of system and already well known in literature (Ghosh et al., 2014; Ebrahimi et al., 2019; Shafiei et al., 2021). The agreements are excellent with respect to the theoretical values. The observed deviations are expected due to

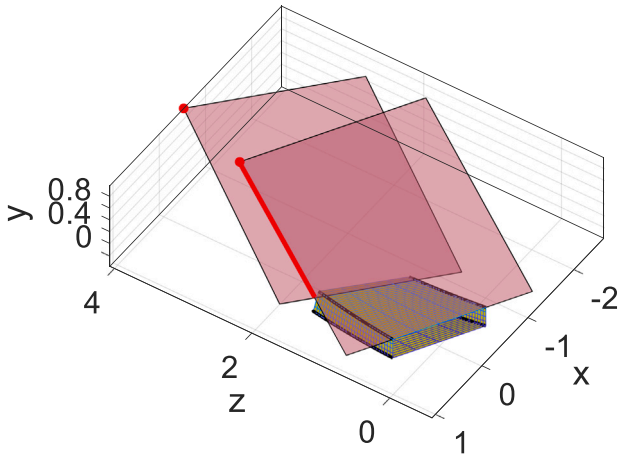

Fig. 9. Visual depiction of the scales in contact at the point of disengagement as scales 'open' up at $\kappa_3 = \kappa_3^*$. (for $\beta = 1.25$, $\alpha = 30°$, $\hat{\kappa}_1 = 0.1$).

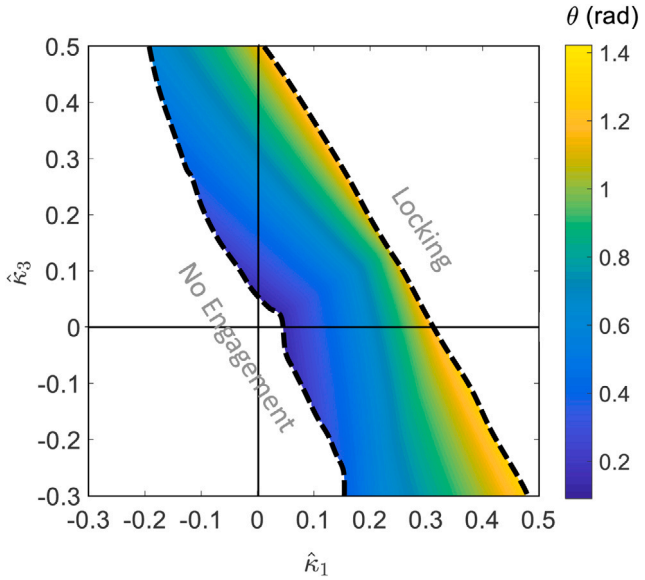

Fig. 10. Slice of the engagement region, Γ_e, as defined in (21) for $\hat{\kappa}_2 = 0$. Points lying inside the shaded region correspond to configurations where scales are in contact. The color bar shows the scale angle θ (in radians) for the corresponding configuration. Here $\theta_0 = 5°$ and $\alpha = 30°$, $\eta = 3$, and $\beta = 1.25$.

the complex nature of the contact, imposing global periodicity, and the difficulties in keeping one curvature constant in an actual numerical simulation due to edge effects.

We see similar and even more dramatic effect in the twist–torque diagram in Fig. 12 (a). Here again, we see the role of the bending strains as the torque–twists, which are smooth nonlinear plots in pure twisting case (Ebrahimi et al., 2019), now turn into highly discontinuous plots with disparate twist modulus. Yet again, an existing bending strain can cause the neutral position (zero-twist strain) to be pre-engaged due to bending. This highlights the appreciable differences that can be brought about from cross-coupling effects. Fig. 12(b) shows the companion FE torque–twist plots that also indicate excellent agreement with the analytical results. As in the case of bending, the deviations are mainly because of the difficulties in keeping the cross curvatures fixed for the simulation duration. The other errors are possibly due to assuming fixed curvatures as opposed to spatially varying curvatures arising in a FE simulation. Analogous to bending case, imposing global periodicity in scale engagements also leads to some differences in behavior. Please note that many of these non-ideal effects and sources of discrepancies have been discussed earlier (Ghosh et al., 2017; Ali et al., 2019a).

5. Conclusions

In this work, we addressed the cross coupling effects of bending and twisting in a biomimetic scale elastic beam for the first time. Here the scales were plate like rectangular inclusions protruding at an angle from the surface of the elastic substrate. We find highly intricate and often surprising effect of one over the other across the kinematics and mechanics. We quantified these effects

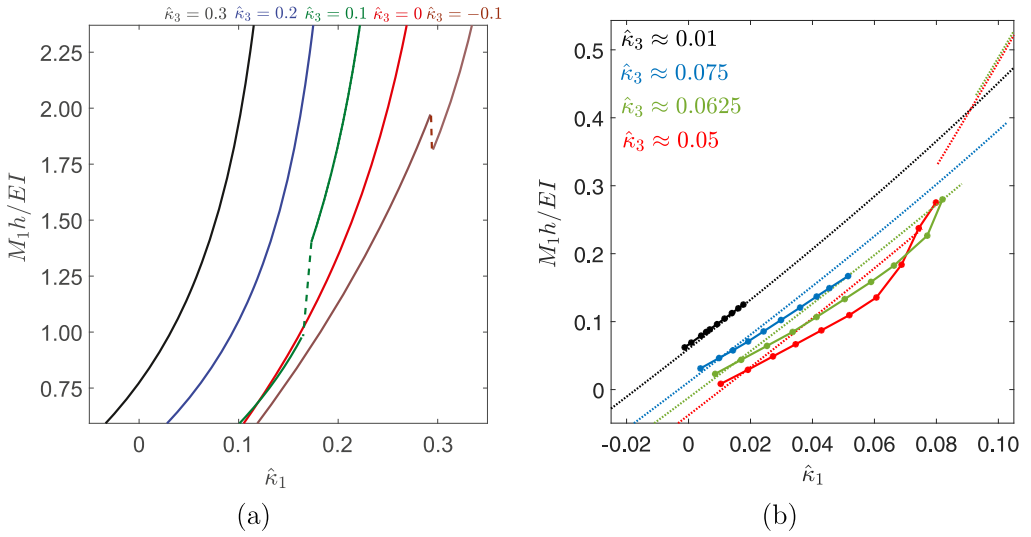

Fig. 11. Bending moment M_1 versus $\hat{\kappa}_1$ for various values of $\hat{\kappa}_3$: (a) Plots for the analytical model. (b) Plots using FE analysis as solid lines with point markers lines comparing with theoretical results as dotted lines.

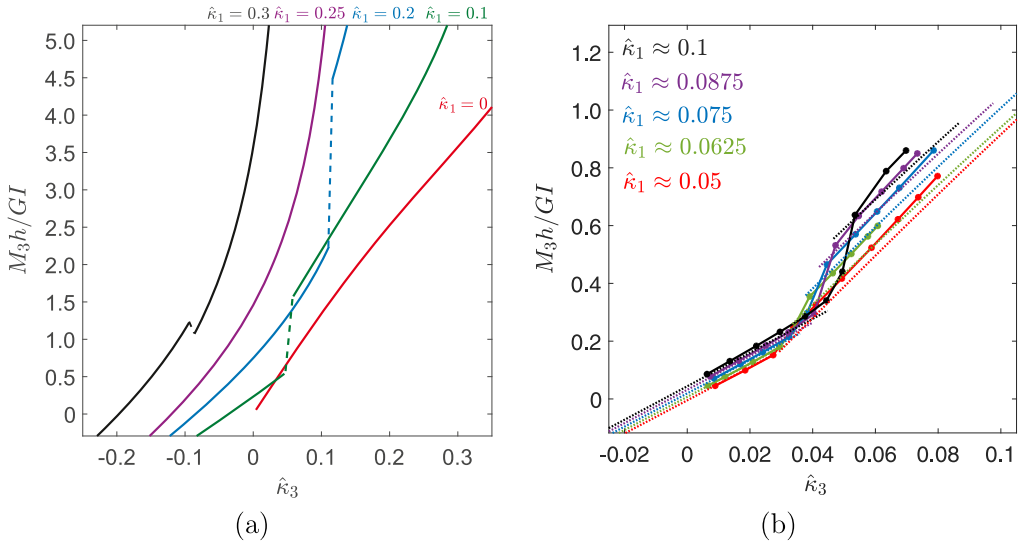

Fig. 12. Twisting moment M_3 versus $\hat{\kappa}_3$ for various values of $\hat{\kappa}_1$: (a) Plots for the analytical model. (b) Plots using FE analysis as solid lines with point markers lines comparing with theoretical results as dotted lines.

by developing analytical relationships within the framework of Cosserat kinematics and global–local energy balance. This model reduced to the earlier developed model for pure bending (Ghosh et al., 2014), and twisting (Ebrahimi et al., 2019) in literature and was also validated with FE simulations. This current study therefore comprehensively considers the effect of combined bending and twisting on scaled elastic beams. The study explains the previously unknown cross-coupling effects. These include novel locking states and greater stiffness gains via cross terms. Specifically, we find that contacts modes can abruptly change, that lead to discontinuous changes in the moment–curvature behavior. We also found that the cross-coupling sensitivities were not symmetric and there exists a distinct engagement regime of operation sandwiched between region of no contact and kinematically forbidden region. Such cross-coupling terms significantly open design space and at the same time warn us of unwanted stiffness changes due to geometric defects. These models can thus help in both design and optimization of these structures for specific applications that depend on variable stiffness beams and filaments such as soft robotics. At the same time this study does not cover inhomogeneous scale distributions. Bending behavior of substrates with of inhomogeneous stiff scale distributions including functional gradation has been covered earlier (Ali et al., 2019a,c). In those studies, it was shown that although calculations are significantly more complicated, the results vis-à-vis locking and nonlinear stiffening still hold.

This study also does not consider scale deformation in combined loading. However, the effect of some scale deformation has been considered earlier for bending and twisting individually (Ghosh et al., 2017; Vernerey and Barthelat, 2014; Vernerey et al., 2014). We consider the current paper as an important starting point for extension into more complex scale materials and deformations. We have

also neglected inter-scale friction for this study, which will be treated in a future work. The contact algorithm used in this problem has been chosen for ease of formulation, and other techniques can be used for this purpose, although the ultimate mechanics results may not change appreciably. Finally, the computational tools that can handle fish scale type problems that involve large number of contacts are still lagging behind. Commercial FE has severe limitations which prohibit large deflection simulations. Several advances have been made in the recent past which could eventually help this problem (Vernerey et al., 2014; Shafiei et al., 2021). Of specific significance are the approaches that homogenize the scale interactions with periodic constraints resulting in nonlinear membrane response in bending or twisting suitable for FE implementation (Vernerey et al., 2014).

Declaration of competing interest

The authors declare that they have no known competing financial interests or personal relationships that could have appeared to influence the work reported in this paper.

Acknowledgment

This work was supported by the United States National Science Foundation's Civil, Mechanical, and Manufacturing Innovation, CAREER Award #1943886.

Appendix A. Extracting cosserat strains from FE data

To compare the FE simulations with the analytical model presented in Section 2, we extract the Cosserat bending strains κ_1, κ_2, and κ_3 from the FE data through the following steps. First, we extract the position vector for the mid-point of the top face of the beam from the numerical simulations. This vector is an estimate for $\mathbf{r}(s)$ as given in (8). The information of the directors $\mathbf{d}_1(s)$ and $\mathbf{d}_2(s)$ is extracted by subtracting the position vectors of center-line and the right-edge of the beam, respectively, from the estimate for $\mathbf{r}(s)$ and normalizing the resulting quantities to produce unit vectors. After validating inextensibility by verifying that the change in length of the rod is small (with typical percentage relative error $\Delta L_B/L_B \approx 1\%$), we compute the third director using $\mathbf{d}_3 = \mathbf{r}'(s)$, estimating the right hand side using finite differences along the beam. It follows from (1) that rotation matrix mapping the cross-sections of the beam is given by $\mathbf{Q}(s) = [\mathbf{d}_1(s), \mathbf{d}_2(s), \mathbf{d}_3(s)]$ where the directors are taken to be the column vectors of the matrix. The skew-symmetric matrix $\mathbf{K}$ containing the bending strains $\kappa_1(s)$, $\kappa_2(s)$, $\kappa_3(s)$ (cf. (4)) along the length of the beam is computed using the formula $\mathbf{K} = \mathbf{Q}'(s)\mathbf{Q}^{-1}(s)$, where $\mathbf{Q}'(s)$ is estimated using finite differences. To avoid boundary effects, we average the bending strains over the middle half of the beam to obtain estimates for average bending strains in the beam (see Fig. A.13).

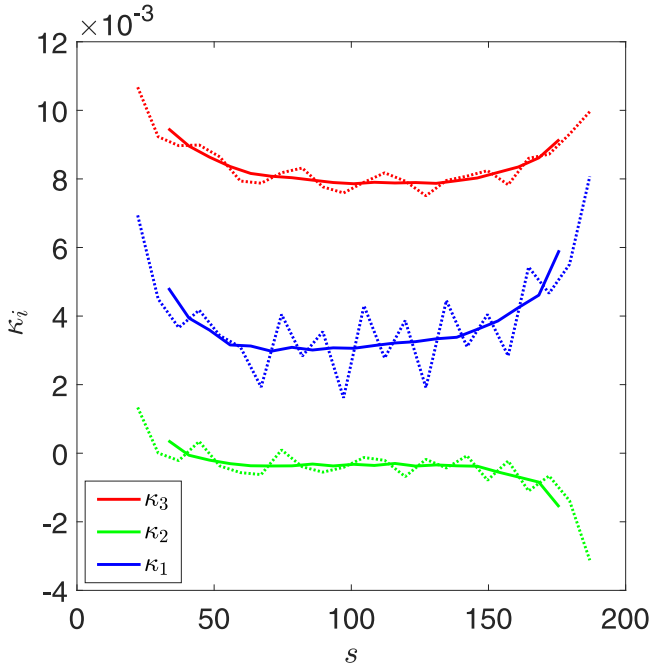

Fig. A.13. Extracting Cosserat strain from FE Data.

Appendix B. Supplementary data

Supplementary material related to this article can be found online at https://doi.org/10.1016/j.jmps.2021.104711.

References

Abaqus, V., 2014. 6.14 Documentation. Dassault Systemes Simulia Corporation 651 (6.2).

Ali, H., Ebrahimi, H., Ghosh, R., 2019a. Bending of biomimetic scale covered beams under discrete non-periodic engagement. Int. J. Solids Struct. 166, 22–31.

Ali, H., Ebrahimi, H., Ghosh, R., 2019b. Frictional damping from biomimetic scales. Sci. Rep. 9 (1), 14628.

Ali, H., Ebrahimi, H., Ghosh, R., 2019c. Tailorable elasticity of cantilever using spatio-angular functionally graded biomimetic scales. Mech. Soft Mater. 1, 10.

Ali, H., Ebrahimi, H., Stephen, J., Warren, P., Ghosh, R., 2020. Tailorable stiffness lightweight soft robotic materials with architectured exoskeleton. In: AIAA Scitech 2020 Forum. p. 1551.

Antman, S.S., 1995. Nonlinear Problems of Elasticity. Springer.

Audoly, B., Pomeau, Y., 2010. Elasticity and Geometry: From Hair Curls to the Non-Linear Response of Shells. Oxford University Press.

Buehler, M.J., 2006. Nature designs tough collagen: explaining the nanostructure of collagen fibrils. Proc. Natl. Acad. Sci. 103 (33), 12285–12290.

Chang, W., Bloch, R., Tschoegl, N., 1976. Time-dependent response of soft polymers in moderately large deformations. Proc. Natl. Acad. Sci. 73 (4), 981–983.

Chen, I.H., Kiang, J.H., Correa, V., Lopez, M.I., Chen, P.-Y., McKittrick, J., Meyers, M.A., 2011. Armadillo armor: mechanical testing and micro-structural evaluation. J. Mech. Behav. Biomed. Mater. 4 (5), 713–722.

Ebrahimi, H., Ali, H., Ghosh, R., 2020. Coulomb friction in twisting of biomimetic scale-covered substrate. Bioinspiration Biomim. 15 (5), 056013.

Ebrahimi, H., Ali, H., Horton, R.A., Galvez, J., Gordon, A.P., Ghosh, R., 2019. Tailorable twisting of biomimetic scale-covered substrate. Europhys. Lett. 127 (2), 24002.

Ebrahimi, H., Ali, H., Stephen, J., Dharmavaram, S., Ghosh, R., 2021a. Emergent mechanical properties of biomimetic exoskeletal metamaterials. In: Bioinspiration, Biomimetics, and Bioreplication XI, Vol. 11586. International Society for Optics and Photonics, p. 115860N.

Ebrahimi, H., Ali, H., Stephen, J., Ghosh, R., 2021b. Fish scales: Primitive basis for modern metamaterials. Europhys. Lett. 133 (6), 68001.

Ghosh, R., Ebrahimi, H., Vaziri, A., 2014. Contact kinematics of biomimetic scales. Appl. Phys. Lett. 105 (23), 233701.

Ghosh, R., Ebrahimi, H., Vaziri, A., 2016. Frictional effects in biomimetic scales engagement. Europhys. Lett. 113 (3), 34003.

Ghosh, R., Ebrahimi, H., Vaziri, A., 2017. Non-ideal effects in bending response of soft substrates covered with biomimetic scales. J. Mech. Behav. Biomed. Mater. 72, 1–5.

Kemoole, J., 2017. Online Image, Flickr, (accessed September 5, 2020), URL https://flic.kr/p/YSe1Us.

Kertész, K., Molnár, G., Vértesy, Z., Koós, A., Horváth, Z., Márk, G., Tapasztó, L., Bálint, Z., Tamáska, I., Deparis, O., et al., 2008. Photonic band gap materials in butterfly scales: A possible source of “blueprints”. Mater. Sci. Eng. B 149 (3), 259–265.

LaTorre, C., Bhushan, B., 2006. Investigation of scale effects and directionality dependence on friction and adhesion of human hair using AFM and macroscale friction test apparatus. Ultramicroscopy 106 (8–9), 720–734.

Long, J., Hale, M., Mchenry, M., Westneat, M., 1996. Functions of fish skin: flexural stiffness and steady swimming of longnose gar, lepisosteus osseus. J. Exp. Biol. 199 (10), 2139–2151.

Martini, R., Balit, Y., Barthelat, F., 2017. A comparative study of bio-inspired protective scales using 3D printing and mechanical testing. Acta Biomater. 55, 360–372.

Michielsen, K., Stavenga, D., 2008. Gyroid cuticular structures in butterfly wing scales: biological photonic crystals. J. R. Soc. Interface 5 (18), 85–94.

Roche, E.T., Horvath, M.A., Wamala, I., Alazmani, A., Song, S.-E., Whyte, W., Machaidze, Z., Payne, C.J., Weaver, J.C., Fishbein, G., et al., 2017. Soft robotic sleeve supports heart function. Sci. Transl. Med. 9 (373), eaaf3925.

Sadati, S.H., Noh, Y., Naghibi, S.E., Kaspar, A., Nanayakkara, T., 2015. Stiffness control of soft robotic manipulator for minimally invasive surgery (mis) using scale jamming. In: International Conference on Intelligent Robotics and Applications. Springer, pp. 141–151.

Shafiei, A., Pro, J.W., Martini, R., Barthelat, F., 2021. The very hard and the very soft: Modeling bio-inspired scaled skins using the discrete element method. J. Mech. Phys. Solids 146, 104176.

Sheen, S.H., Larionov, E., Pai, D.K., 2021. Volume preserving simulation of soft tissue with skin. Proceedings of the ACM on Computer Graphics and Interactive Techniques 4 (3), 1–23.

Sire, J.-Y., Donoghue, P.C., Vickaryous, M.K., 2009. Origin and evolution of the integumentary skeleton in non-tetrapod vertebrates. J. Anat. 214 (4), 409–440.

Song, J., Reichert, S., Kallai, I., Gazit, D., Wund, M., Boyce, M.C., Ortiz, C., 2010. Quantitative microstructural studies of the armor of the marine threespine stickleback (Gasterosteus aculeatus). J. Struct. Biol. 171 (3), 318–331.

Ugural, A.C., Fenster, S.K., 2011. Advanced Mechanics of Materials and Applied Elasticity. Pearson Education.

Vernerey, F.J., Barthelat, F., 2010. On the mechanics of fishscale structures. Int. J. Solids Struct. 47 (17), 2268–2275.

Vernerey, F.J., Barthelat, F., 2014. Skin and scales of teleost fish: Simple structure but high performance and multiple functions. J. Mech. Phys. Solids 68, 66–76.

Vernerey, F.J., Musiket, K., Barthelat, F., 2014. Mechanics of fish skin: A computational approach for bio-inspired flexible composites. Int. J. Solids Struct. 51 (1), 274–283.

Wang, B., Yang, W., Sherman, V.R., Meyers, M.A., 2016. Pangolin armor: overlapping, structure, and mechanical properties of the keratinous scales. Acta Biomater. 41, 60–74.

Wegst, U.G., Bai, H., Saiz, E., Tomsia, A.P., Ritchie, R.O., 2015. Bioinspired structural materials. Nature Mater. 14 (1), 23–36.

Wei, Y., Chen, Y., Ren, T., Chen, Q., Yan, C., Yang, Y., Li, Y., 2016. A novel, variable stiffness robotic gripper based on integrated soft actuating and particle jamming. Soft Robot. 3 (3), 134–143.

Yang, L., Yang, L., Lowe, R.L., 2021. A viscoelasticity model for polymers: Time, temperature, and hydrostatic pressure dependent Young’s modulus and Poisson’s ratio across transition temperatures and pressures. Mech. Mater. 157, 103839.